Paranodal myelin retraction in relapsing experimental autoimmune encephalomyelitis visualized by coherent anti-Stokes Raman scattering microscopy

Yan Fu
Terra J. Frederick
Terry B. Huff
Gwendolyn E. Goings
Stephen D. Miller
Ji-Xin Cheng

Paranodal myelin retraction in relapsing experimental autoimmune encephalomyelitis visualized by coherent anti-Stokes Raman scattering microscopy

Yan Fu,[a] **Terra J. Frederick,**[b] **Terry B. Huff,**[c] **Gwendolyn E. Goings,**[b] **Stephen D. Miller,**[b] **and Ji-Xin Cheng**[a,c]
[a]Purdue University, Weldon School of Biomedical Engineering, 206 South Martin Jischke Drive, West Lafayette, Indiana 47907
[b]Northwestern University Medical School, Department of Microbiology-Immunology and the Interdepartmental Immunobiology Center, 303 East Chicago Avenue, Chicago, Illinois 60611
[c]Purdue University, Department of Chemistry, West Lafayette, Indiana 47907

Abstract. How demyelination is initiated is a standing question for pathology of multiple sclerosis. By label-free coherent anti-Stokes Raman scattering (CARS) imaging of myelin lipids, we investigate myelin integrity in the lumbar spinal cord tissue isolated from naïve SJL mice, and from mice at the onset, peak acute, and remission stages of relapsing experimental autoimmune encephalomyelitis (EAE). Progressive demyelinating disease is initially characterized by the retraction of paranodal myelin both at the onset of disease and at the borders of acute demyelinating lesions. Myelin retraction is confirmed by elongated distribution of neurofascin proteins visualized by immunofluorescence. The disruption of paranodal myelin subsequently exposes Kv1.2 channels at the juxtaparanodes and lead to the displacement of Kv1.2 channels to the paranodal and nodal domains. Paranodal myelin is partially restored during disease remission, indicating spontaneous myelin regeneration. These findings suggest that paranodal domain injury precedes formation of internodal demyelinating lesions in relapsing EAE. Our results also demonstrate that CARS microscopy is an effective readout of myelin disease burden. © 2011 Society of Photo-Optical Instrumentation Engineers (SPIE). [DOI: 10.1117/1.3638180]

Keywords: experimental autoimmune encephalomyelitis; paranodal myelin; demyelination; remyelination; potassium channels; neurofascin proteins; coherent anti-Stokes Raman scattering microscopy.

1 Introduction

Myelinated axons allow the action potentials to be generated at nodes of Ranvier and signals to propagate in a saltatory pattern. The lateral borders of the myelin sheath connect with axolemma at paranodes through the axon-glial junctions,[1] which segregate Na^+ channels at the nodes and K^+ channels at the juxtaparanodes along the axolemma.[2] Specialized axo-glial junctions at the paranodes include oligodendrocyte transmembrane protein neurofascin 155 and axonal adhesion molecules Caspr-1 and contactin.[3,4] High-density Na^+ channels assemble at the node through interactions with proteins including neurofascin 186 (Refs. [5] and [6]) in the axolemma. K^+ channels located at the juxtaparanodes are covered by a compact myelin sheath. The integrity of nodal and paranodal domains is vital to fast-action potential conduction along myelinated axons. Studies have shown that disruption of neurofascin localization precedes demyelination in tissues from multiple sclerosis (MS) patients,[7] and that disruption of the axonal contactin-associated protein (Caspr)-1 may be an indicator of myelin abnormalities.[8] Moreover, diffusive patterns of Kv1.2, paranodin, Caspr-2, and Nav channels were found in immunolabeled plaques from MS patients.[9] Nevertheless, due to lack of control of the disease stages in these studies using MS tissues, it is not clear whether

paranodal domain injury occurs at the onset of the disease. More importantly, the status of paranodal and nodal myelin at different stages of the disease was not clarified due to lack of a proper myelin observation tool.

In this paper, we address the above issues by a thorough imaging study of myelin in relapsing experimental autoimmune encephalomyelitis (R-EAE), a widely used animal model reproducing specific features of the histopathology and neurobiology of MS. Accepted as a T-cell-mediated autoimmune disease of the central nervous system,[10] the EAE model has been extensively employed for investigation into the mechanisms of myelin loss[11,12] and assessment of myelin repair therapies.[13,14] Myelin is normally characterized by electron microscopy (EM) and/or histology. Although EM provides ultrastructure of myelin in resin-embedded sections, its sophisticated sample preparation and small field of view inhibit effective quantitative and/or statistical examination. Luxol fast blue staining of paraffin-embedded tissues is a widely used histological method for large-area mapping of the white matter. However, this method lacks the resolution for observation of changes in single myelin tracks, which inhibits unequivocal discrimination of remyelination from normal myelination. Clinical imaging tools, including magnetic resonance imaging and positron-emission tomography, permit noninvasive longitudinal imaging of the central nervous system and demyelinating lesions in the white matter,[15,16] but only at a low spatial resolution that is

Address all correspondence to: Ji-Xin Cheng, Purdue University, Weldon School of Biomedical Engineering, 206 South Martin Jischke Drive, West Lafayette, Indiana 47907; Tel: 765-494-4335; Fax: 765-496-1912; E-mail: jcheng@purdue.edu.

insufficient to reveal details at the single myelin track level. Currently, a correlation between myelin status and clinical scores of EAE is missing. In particular, characterization of the nature of the initial damage to myelin at disease onset remains unclear. A dearth of such knowledge has slowed the use of EAE for mechanistic studies of myelin loss, as well as therapeutic development of myelin repair strategies.

By providing contrast based on C–H bond vibration,[17] coherent anti-Stokes Raman scattering (CARS) microscopy has permitted high-speed imaging of natural and chemically damaged myelin in *ex vivo* tissues.[18–22] The CARS contrast arises from the CH_2 symmetric vibration in myelin lipid, which comprises 70% of the dry weight of white matter. As a nonlinear optical process, CARS provides inherent 3-D submicron resolution enabling visualization of detailed myelin structures such as the paranodal myelin loops.[18] In this study, we employ CARS microscopy, coupled with two-photon excited fluorescence (TPEF) imaging and confocal Raman spectral analysis,[23] to distinguish the myelin sheath in naïve mice, and mice during the peak acute and remission stages of R-EAE. We show that paranodal myelin disruption corresponds to the onset of $CD4^+$ T-cell-mediated EAE and is partially restored in the remission stage.

2 Materials and Methods

2.1 Induction of Relapsing Experimental Autoimmune Encephalomyelitis

Female SJL mice were purchased from the Harlan Laboratory (Indianapolis, Indiana) and maintained according to protocols approved by the Northwestern University Animal Care and Use Committee. Mice were primed subcutaneously with an emulsion containing 100 μL of incomplete Freund adjuvant (Difco, Detroit, Michigan) supplemented with 200 μg of *Mycobacterium tuberculosis* H37Ra (Difco, Detroit, Michigan) and 50 μg of $PLP_{139–151}$ (HCLGKWLGHPDKF), which was synthesized by Genemed synthesis. Clinical scores were recorded daily using a scale of 0–5 (0, healthy; 1, limp tail or hind limb weakness; 2, limp tail and hind limb weakness; 3, partial hind limb paralysis; 4, total hind limb paralysis; and 5, moribund). All animal procedures were conducted in complete compliance with the NIH Guide for the Care and Use of Laboratory Animals and were approved by the Institutional Animal Care and Use Committee of Northwestern University.

2.2 Tissue Preparation

SJL mice were anesthetized with sodium pentobarbitol. During deep anesthesia, the mice were perfused transcardially with 10 mL of cold PBS (pH 7.4), and then with 10 mL of PBS containing 4% paraformaldehyde for *in vivo* fixation. The vertebrae were immediately excised and kept in 4% paraformaldehyde. After 24 h, <1-cm-long lumbar spinal cord was extracted and sectioned longitudinally into 100-μm slices from ventral to dorsal side using a tissue slicer (OTS-4000, Electron Microscopy Sciences, Hatfield, Pennsylvania). The slices were stored in PBS prior to imaging. For both ventral and dorsal parts, sliced slices at the same depth were used for comparison between the four groups composed of naïve mice, mice at onset of R-EAE, mice at peak acute of R-EAE, and mice at remission

of R-EAE. For nuclei staining, the fixed spinal cord slices were incubated in PBS supplemented with 4 ng/mL Hoechst33342 dye for 2 h and washed with PBS prior to imaging.

2.3 Coherent Anti-Stokes Raman Scattering and Two-Photon Excited Fluorescence Imaging

Two beams at frequency ω_p and ω_s generated from two tightly synchronized Ti:sapphire lasers (Mira 900/Sync-lock, Coherent Inc., Santa Clara, California), with a pulse duration of 2.5 ps, were used for both CARS and TPEF imaging on the same microscope. The two beams were parallel polarized and collinearly combined. A Pockels' cell was used to reduce the repetition rate from 78 to 7.8 MHz. The overlapping beams were directed into a laser-scanning microscope (FV300/IX70, Olympus Inc., Center Valley, Pennsylvania) and focused into a sample through a 60× water-immersion objective lens [numerical aperture (NA) = 1.2] or a 20× air-objective lens (NA = 0.75). The CARS signal was collected in the forward direction with an air-objective lens (NA = 0.5). The frequency difference between the pump and Stokes beams, $\omega_p - \omega_s$, was tuned to the symmetric CH_2 vibration at 2840 cm^{-1}. The same picosecond laser beams were also used for TPEF imaging of Hoechst or immunofluorescence. The TPEF signal was collected in the backward direction. Both CARS and TPEF signals were detected with the same type of photomultiplier tube (PMT, R3896, Hamamatsu, Japan). No photodamage to myelin was observed.

2.4 Confocal Raman Microspectroscopy

On the CARS microscope, a spectrometer equipped with an electron multiplying charge-coupled device (EMCCD) was attached to the side port with the slit replaced with a pinhole for confocal Raman analysis. After a CARS image was taken, the Stokes beam was blocked and a short-pass dichroic mirror directed the Raman signal into the spectrometer. The point-scan signal from the scanner externally triggered the spectrometer, which recorded a Raman spectrum at a point of interest. A detailed description can be found in elsewhere.[23]

2.5 Immunohistochemistry

Antiserum against Kv1.2 antibody (Alomone Lab, Jerusalem, Israel) was used to locate the K^+ channels at the juxtaparanodes. NFC2 antibody (provided by Professor Peter J. Brophy[3]) was used to label Neurofascin NF155 at the paranodal myelin and neurofascin 186 at the axolemma. Antiserum against F4/80 (Invitrogen, Carlsbad, California) was used to label activated microglia and infiltrated macrophages. FITC conjugated antiserum against CD4 (Ebioscience, San Diego, California) was used to label $CD4^+$ regulatory T cells. Platelet-derived growth factor receptor α (PDGFRα) antibody (Fitzgerald Industries International, Concord, Massachusetts) was used to label oligodendrocyte precursor cells. FITC conjugated anti-rat IgG (Sigma, St. Louis, Missouri) and Alex 488 conjugated anti-rabbit IgG (Sigma, St. Louis, Missouri) were used as secondary antibodies. The immunofluorescence images were taken by TPEF on the same laser-scanning CARS microscope.
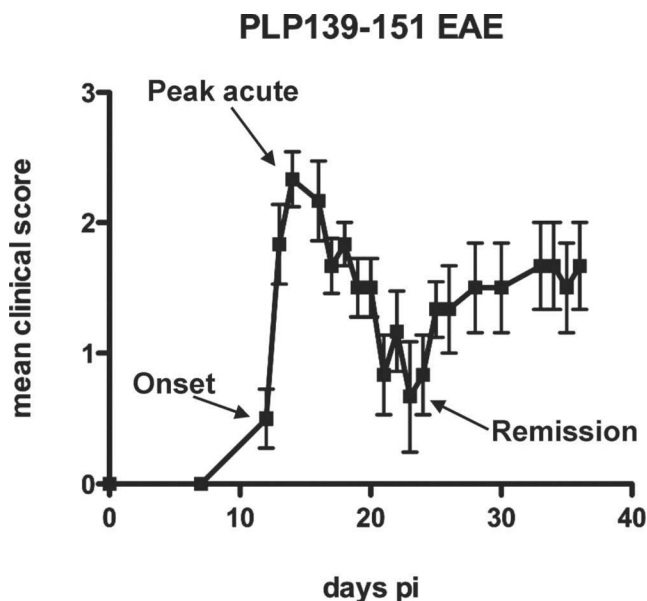
PLP139-151 EAE

Fig. 1 Typical time course of clinical scores for R-EAE mice. The mice at the onset of disease (score of 1 following a period of no clinical symptom after time of immunization), the peak acute (score of 3), and the remission stage (score of 1 following the peak acute), indicated by arrows, were used for the CARS imaging study.

2.6 Statistical Analysis

The statistical data are presented as mean $\pm$ s.d. ANOVA analysis of variance with Tukey's test was used for multiple comparisons within a group. The data in one group were obtained from at least six spinal cord slices, which came from three separate animals.

3 Results

3.1 Multimodal Coherent Anti-Stokes Raman Scattering Imaging Reveals De- and Remyelination in Relapsing Experimental Autoimmune Encephalomyelitis

R-EAE (Fig. 1) was induced by immunizing SJL mice with PLP$_{139-151}$ peptide emulsified in complete Freund's adjuvant, and lumbar spinal cords were extracted at various stages during the disease. White matter in naïve mice, and mice at onset, peak acute, and remission stages of R-EAE was characterized by simultaneous CARS imaging of myelin and TPEF imaging of Hoechst-labeled cellular nuclei. The white matter from a naïve mouse (disease score = 0) showed strong CARS (red) and TPEF (green) signals [Fig. 2(a)], which represent ordered parallel myelin fibers and nuclei of glial cells [Fig. 2(b)], respectively. At the onset of EAE (defined by a disease score of 1 following a period of no clinical symptoms from the time of immunization), which manifests in mice as tail weakness, the myelin in the white matter appeared normal with fibrous structure, but the number of cell nuclei in the lumbar spinal cord was increased significantly compared to naive mice [Figs. 2(c) and 2(d)]. Immunofluorescence imaging showed a large number of CD4$^+$ and F4/80$^+$ immune cells in the meninges of the spinal cord (Fig. 3), indicating the infiltration of T cell and macrophage into the spinal cord during EAE onset. At the peak acute stage of EAE (score = 3 or 4), characterized by partial or complete hind-limb paralysis, demyelinating lesions [Fig. 2(e)] were observed near the meninges of the spinal cord and around blood vessels and were distinguished by extensive myelin debris and clustered cells [Fig. 2(f)]. CARS and two-photon excited immunofluorescence imaging further showed that CD4$^+$ T cells and F4/80$^+$ macrophage/microglia occupied these lesions (Fig. 3). During remission from acute disease (defined by a disease score of 1 following a previous peak score of 3–4), clusters of cells were observed in the meninges of the spinal cord and around blood vessels [Fig. 2(g)]. Adjacent to the accumulated cells, we also observed myelin fibers, small vesicles [arrows in Fig. 2(h)], and randomly organized cells. Combined CARS imaging of myelin and immunofluorescence imaging of labeled PDGFRα showed the existence of oligodendrocyte precursor cells among the randomly organized cells (Fig. 4), consistent with an interpretation of attempted myelin regeneration in these sites. The same types of myelin morphological changes were observed between the dorsal and ventral parts of lumbar spinal tissue extracted from the R-EAE mice. The multimodal images enabled us to quantify the density of myelin fibers, density of cell nuclei, and myelin fiber thickness in each stage of R-EAE. At disease onset, the density of cells in the white matter [e.g., on the left of the dash line in Fig. 2(d)] was almost twice of that in the naïve white matter. In acute lesions, the density of cells increased by 11 times, whereas no intact myelin fibers were identified. In accordance with the incomplete functional recovery in the remission stage (Fig. 1), the density of remyelinated fibers was found to be lower than that in the naïve white matter [Fig. 2(i)]. Moreover, axon diameter and myelin thickness were measured through the intensity profile of CARS signal from the myelin fiber. The regenerated myelin fibers were found thinner [Fig. 2(j)] in both dorsal and ventral parts of spinal cord and overall exhibited a significantly decreased ratio of myelin thickness to the axonal diameter (0.32 $\pm$ 0.13) compared to normal myelin fibers (0.60 $\pm$ 0.25) in the naïve white matter [Fig. 2(k)]. We note that the ratio of myelin thickness to the axonal diameter from normal mice presented here is not equivalent to the g ratio defined as the ratio of the inner diameter to the outer diameter of myelin fiber.

3.2 Raman Spectral Analysis Shows Degradation of Myelin Lipids

To identify conformational and/or chemical changes in naïve, degraded, and regenerated myelin, we recorded Raman spectra of myelin at the different stages of R-EAE by combination of CARS microscopy and confocal Raman microspectroscopy on the same platform.[23] CARS imaging was used to locate the normal myelin in the naïve white matter [Fig. 5(a)], myelin debris in the demyelinating lesions [Fig. 5(b)], and regenerated myelin during the remission [Fig. 5(c)]. The Raman spectra of myelin shown in Fig. 5(d) were dominated by vibrational bands from lipids[24,25] due to the high lipid content in myelin. The spectral assignment and the intensity ratios between the Raman bands are summarized in Tables 1 and 2, respectively. Both the C–C and C–H vibrational bands were used for determining the conformation of the hydrocarbon chains of lipids. We first studied lipid packing using the prominent bands at 2850, 2885, and 2930 cm^{-1}, which correspond to symmetric CH$_2$ stretching, asymmetric CH$_2$ stretching, and CH$_3$ stretching vibrations, respectively. As
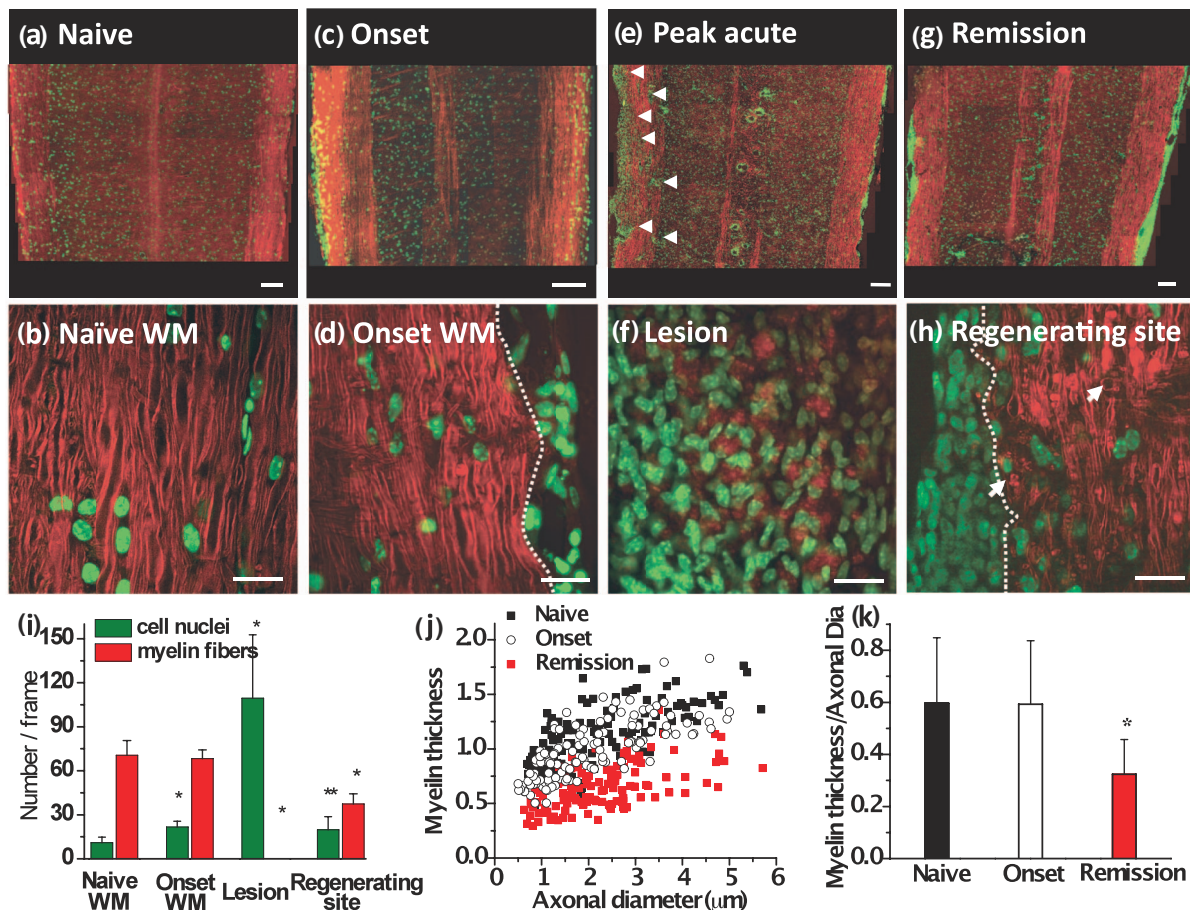
Fig. 2 Multimodal imaging of de- and remyelination in R-EAE. Red: myelin imaged by CARS microscopy; Green: Hoechst-labeled cell nuclei imaged by TPEF. (a) A mosaic image shows a large view of a lumbar spinal cord slice from a naïve mouse. (b) A magnified image displays parallel myelinated fibers and regularly organized cellular nuclei in the naive white matter. (c) A mosaic image shows a large view of a lumbar spinal cord slice from a R-EAE mouse at disease onset. (d) Parallel myelin fibers adjacent to the infiltrated cells at R-EAE onset. (e) A mosaic image shows a large view of a lumbar spinal cord slice at the peak acute stage of R-EAE. Demyelinating lesions are indicated by arrow heads. (f) Clusters of cells and myelin debris in a demyelinating lesion. (g) A mosaic image shows a large view of a lumbar spinal cord slice at the remission stage of R-EAE. Numerous cells are restricted in the meninges of the spinal cord and around blood vessels. (h) Remyelinated fibers in a regenerating site (on the right of the dotted line). The arrows indicate the presence of myelin vesicles. (i) Comparison of myelinated fiber number and cell number per frame of image in the naïve white matter, EAE onset white matter, acute demyelinating lesions, and regenerating sites. The frame size is 0.014 mm^2. *$p < 0.001$, **$p < 0.05$ in comparison to cell nuclei and myelin fibers in the naïve white matter, respectively. (j,k) Comparison of myelin thickness versus axonal diameter at the naïve white matter, white matter at disease onset, and remyelinated fibers at the remission stage. *$p < 0.001$ in comparison to the naïve white matter. In (a), (c), (e), and (g), bar = 100 μm; in (b), (d), (f), and (h), bar = 20 μm.

shown in Fig. 5(e) and Table 2, a significantly larger intensity ratio of I_{2930}/I_{2885} was found in myelin debris, which reflects an increase of the intermolecular chain disorder.[25] Interestingly, the regenerated myelin also showed a higher lipid-packing disorder than the normal myelin. We further studied the lipid unsaturation using the intensity ratio of I_{1650}/I_{1445}, which represents the ratio of C=C stretching vibration bands to H–C–H deformation bands in lipid acyl chains. We found that myelin debris gave the highest unsaturation degree [Fig. 5(e)]. Myelin regeneration decreased the unsaturation degree but remained higher than the normal myelin. Additionally, the intensity ratio of I_{1122}/I_{1076}, which is related to the ratio of the trans and cis conformation populations of C–C bonds, was employed to examine the intramolecular chain ordering in lipid hydrocarbon chains,[24] but no significant difference was observed between the myelin debris, normal myelin, and regenerated myelin. In summary, Raman spectral analysis of lipid conformations shows that the degraded myelin

has lower lipid-packing ordering and higher unsaturation than normal myelin, and that the lipid conformation is not fully recovered in regenerated myelin. The increase of unsaturation in myelin debris might be due to the formation of conjugated double bond systems and the isomerisation of cis to trans double bonds during lipid oxidation.[26] Notably, previous measurements of lipid acyl chain composition using magic angle-spinning NMR spectroscopy also showed an increase of polyunsaturation degree in the cerebral white matter from EAE marmoset.[27]

3.3 Paranodal Myelin Disruption Occurs at Onset of Experimental Autoimmune Encephalomyelitis and within Borders of Demyelinating Lesions

To our surprise, the density of myelin fibers [Fig. 2(i)] and the myelin thickness [Fig. 2(j)] at the onset of EAE showed no difference from those in the naïve white matter. To account for
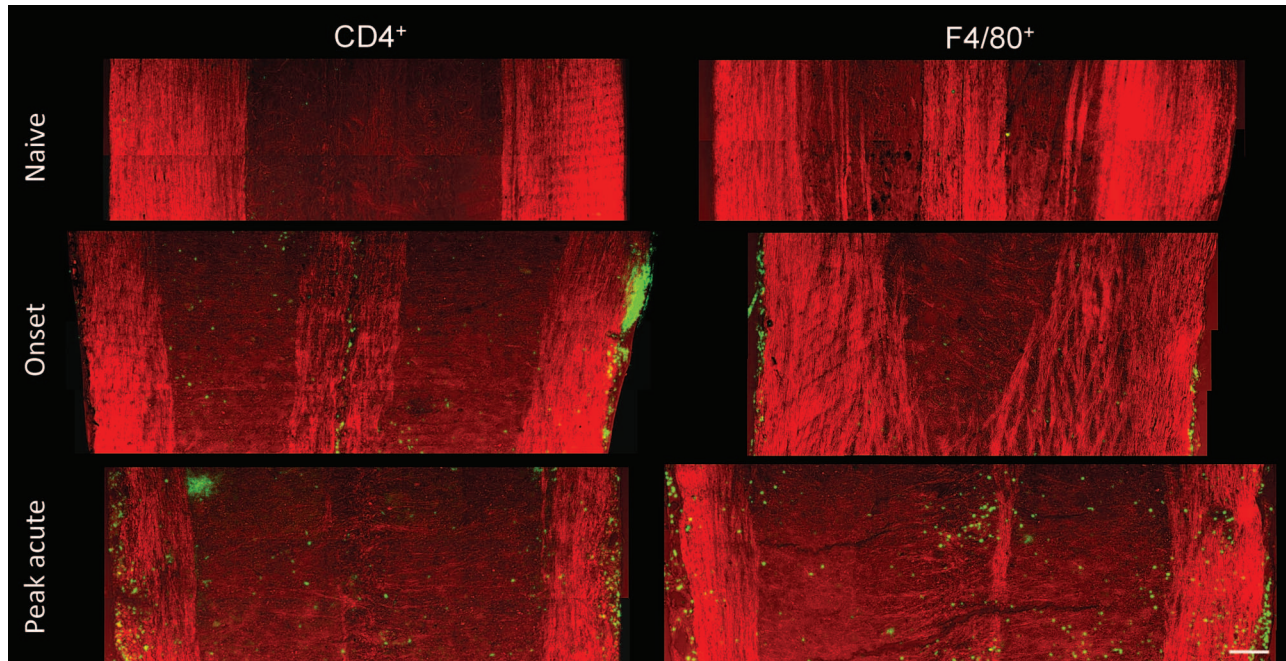
Fig. 3 Mosaic images showing large-view distribution of CD4$^+$ and F4/80$^+$ cells at the lumbar spinal tissues of a naïve mouse, EAE mice at the onset, and peak acute. Bar = 100 μm.

the functional deficit, we examined possible myelin degradation occurring in the paranodal domain. Normally, the paranodal myelin is held on the axolemma by the axo-glial junctions, which segregate the Na$^+$ and K$^+$ channels along the axolemma.[2] Under the CARS microscope, we observed clear differences of paranodal myelin in the lumbar spinal tissues between naïve and R-EAE mice. In the naïve white matter, the node of Ranvier [Fig. 6(a)] was observed as a gap between two segments of myelin sheath. However, in the white matter of EAE spinal cord during onset and within borders of acute demyelinating lesions, a larger distance between two myelin segments was observed [Figs. 6(b) and 6(c)], which indicates a retraction of paranodal myelin toward internodes. To quantify such retraction, we define the nodal diameter as the distance of the CARS signal at the two sides across the axon and nodal length as the distance of the CARS signal at two sides along the axon [Fig. 6(d)]. We measured both nodal length and nodal diameter in the white matter of lumbar spinal tissue at different stages of R-EAE. Our data shown in Figs. 6(e) and 6(f) indicate that the nodal length with the same nodal diameter in the white matter of EAE spinal cord during onset, and within the lesion borders of the peak acute EAE spinal cord is much larger than that in the naïve stage. Moreover, the extent of nodal length increase is not correlated
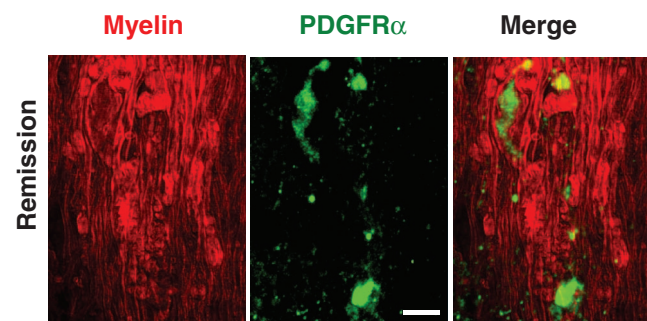
Table 1 Full Raman spectra and assignments of Raman peaks in myelin.

Raman shift, cm^{-1}	Assignment[a]
1057	Trans ν (C–C)
1076	**Gauche ν (C–C)**
1122	**Trans ν (C–C)**
1264	δ (=C–H) in plane cis
1294	δ (CH2) twisting
1431	δ (CH2) bending
1445	**δ (CH2)**
1650	**ν (C=C) cis**
1675	Protein amide I region
2849	CH2 symmetric stretch
2885	**CH2 asymmetric stretch**
2930	**CH3 symmetric stretch**
3009	=C–H symmetric stretch cis

[a]δ and ν indicate deformation and stretching vibration, respectively.

Fig. 4 Presence of oligodendrocyte precursor cells at the remission stage of R-EAE. Red: myelin imaged by CARS; green: immunolabeled PDGFRα imaged by TPEF. Bar = 10 μm.
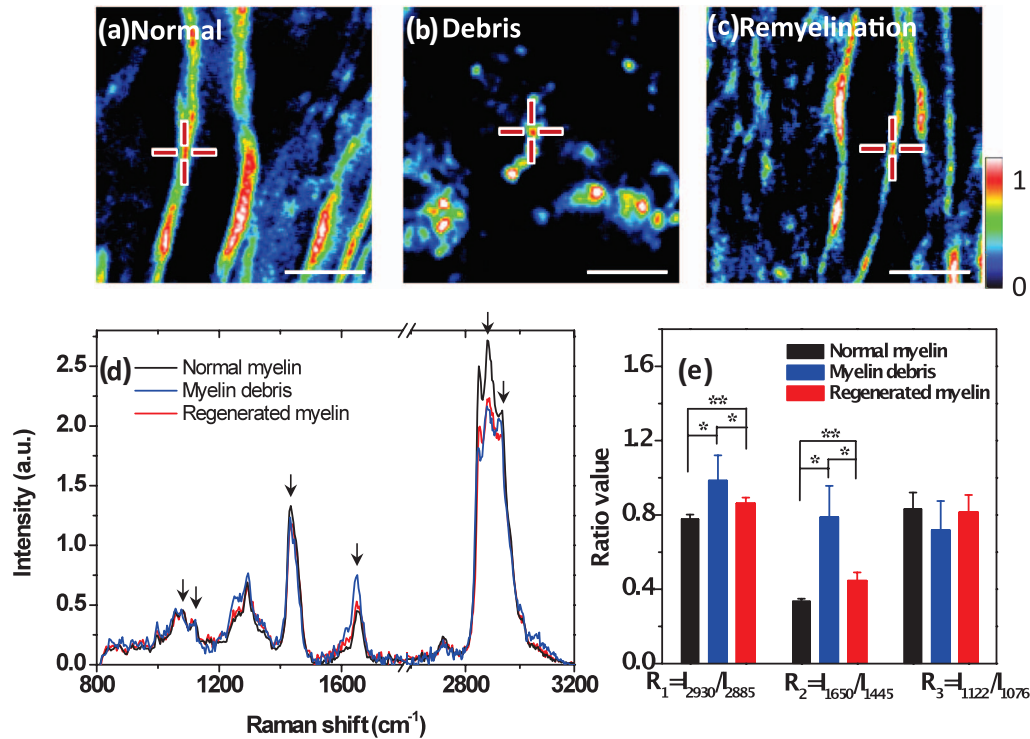
Fig. 5 Confocal Raman spectral analysis of myelin lipid conformation. (a–c) Typical CARS images of normal myelin, myelin debris, and regenerated myelin from lumbar spinal tissues in naïve, peak acute, and remission stages, respectively. The centers of the crosses indicate the positions where Raman spectra are recorded. Bar = 5 μm. (d) Confocal Raman spectra normalized by integral of area under the curves. The peaks at 1076, 1122, 1445, 1650, 2885, and 2930 cm^{-1} from left to right are indicated by black arrows. (e) Histogram comparing the ratios of intensity between different peaks. $*p < 0.005$; $**p < 0.05$.

to the nodal diameter [Fig. 6(f)]. The observation of elongated exposed nodes without loss of segmental myelin indicates that degradation of paranodal myelin occurs prior to the formation of myelin debris.

3.4 Paranodal Myelin Retraction is Associated with Elongated Neurofascin Distribution in Paranodal Domains

To explore molecular changes in the myelin-retracted nodes, we used NFC2 antibody to locate neurofascin155 and neurofascin186. Expression of Neurofascin186 is restricted to neurons and clusters at the nodal membrane.[28] Neurofascin155 is located at the oligodendrocyte loops[3] and functions as a glial receptor for the paranodin/caspr-contactin axonal complex at the axo-glial

junctions.[4] In the naïve white matter, the NFC2 antibody labeled both nodes and paranodes [Fig. 7(a)]. However, in spinal cord white matter from R-EAE mice at onset [Fig. 7(b)] and within acute lesion borders of peak acute spinal cord tissue [Fig. 7(c)], we found that NFC2 labeling extended into the internodes. The extension of NFC2 labeling to the internodes concords with the observation of retracted paranodal myelin shown in Figs. 6(b) and 6(c). Furthermore, by measuring the length of labeled NFC2 at different disease stages, we found that with similar axonal diameter, NFC2 labeling was significantly longer in the spinal cord white matter of EAE mice during disease onset and within acute lesion borders of mice during peak acute EAE, compared to that in white matter isolated from naïve spinal cords [Fig. 7(d)]. The observation of elongated NFC2 labeling further confirms the retraction of paranodal myelin.

Table 2 Intensity ratios for the interested Raman peaks.

	$R_1 = I_{2930}/I_{2885}$	$R_2 = I_{1650}/I_{1445}$	$R_3 = I_{1122}/I_{1076}$
Normal myelin	0.778 ± 0.024 ($n = 13$)	0.336 ± 0.013	0.832 ± 0.089
Myelin debris	0.985 ± 0.136 ($n = 13$)	0.788 ± 0.168	0.717 ± 0.158
Regenerated myelin	0.862 ± 0.031 ($n = 13$)	0.446 ± 0.045	0.814 ± 0.094

R_1 represents the intermolecular chain disorder in lipid hydrocarbon chains.
R_2 represents the lipid-chain unsaturation degree. For example, $R_2 = 0$ for the saturated palmitic acid, $R_2 = 0.58$ for the monounsaturated oleic aid, and $R_2 = 1.27$ for the polyunsaturated linoleic acid (Ref. 23).
R_3 represents the intramolecular chain ordering in lipid hydrocarbon chains.
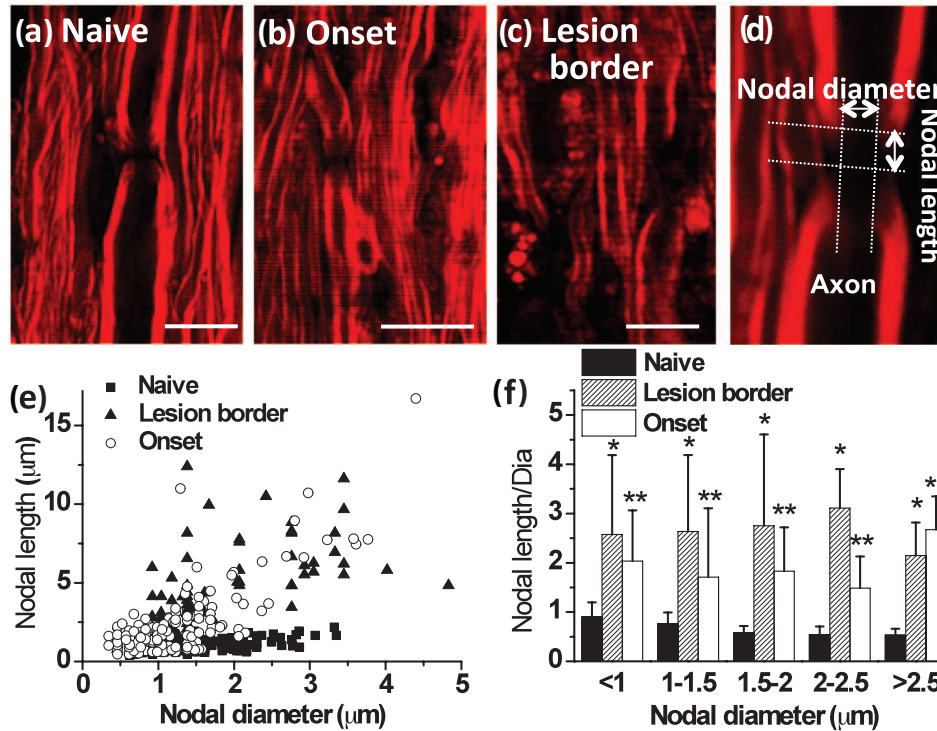
Fig. 6 Paranodal myelin disruption at onset of EAE and within borders of demyelinating lesions. (a–c) Typical CARS images of myelinated nodes in the white matter of a naïve mouse, EAE mice at disease onset, and within borders of demyelinating lesions at the peak acute EAE. A node of Ranvier was observed as a small gap between two segments of compact myelin sheaths in the naïve white matter. Elongated exposure of nodes was observed at locations no more than 100 μm away from the meninges in disease onset and within borders of demyelinating lesions at the peak acute stage. The lesion border was defined as the area extending no more than 100 μm from the locations where the myelin fiber started to appear. The lesions were characterized by myelin debris. (d) Diagram showing the measurement of nodal length and diameter. (e) Nodal lengths versus nodal diameters for myelin at three stages corresponding to (a–c). (f) Comparison of ratios of nodal lengths to nodal diameters at three stages in different nodal diameters. Both *$p < 0.001$ and **$p < 0.001$ are compared to the ratio in the naïve mice from the same range of nodal diameter. Bar = 10 μm.

3.5 Paranodal Myelin Retraction Exposes and Displaces Juxtaparanodal Kv1.2 Channels

The K$^+$ channels,[29] especially the Kv1.1, Kv1.2, and Kvβ2 subunits, are normally located at the juxtaparanodes and protected by myelin.[30,31] To examine the effect of paranodal myelin retraction on the K$^+$ channels, we immunolabeled Kv1.2 channels in the white matter of naïve mice, EAE mice at onset, and EAE mice at the peak acute phase, respectively. A mosaic CARS image of lumbar spinal tissue from mice at peak acute EAE is shown in Fig. 8(a). Similar to that in the naïve white matter [Fig. 8(b)], typical paired immunolabeling of Kv1.2 channels were observed to be located at the juxtaparanodes and concealed beneath compact myelin sheath in the normal-appearing white matter (NAWM) [stars in Fig. 8(c)]. In contrast, exposed Kv1.2 channels were commonly observed at the borders of demyelinating lesions [arrows in Fig. 8(d)] and during disease onset [Fig. 8(f)]. The disruption of paranodal myelin also suggests consequent breakdown of axo-glial junctions between the axon and myelin at the paranodal domain. Accordingly, displacement of Kv1.2 channels into paranodal and nodal domains was observed in the acute lesion borders [Fig. 8(e)] and the white matter of mice with a score of 1 during disease onset [Fig. 8(f)]. In the lesions, no paired Kv1.2 channels were found among myelin debris [Fig. 8(a)]. The disruption of paranodal myelin and consequent exposure and redistribution of K$^+$ channels would definitely impair the saltatory axonal conduction, which could account for the clinical symptoms of EAE at disease onset.

3.6 Paranodal Myelin is Partially Restored in Disease Remission

Using the R-EAE model, we further explored the status of paranodal myelin in the regeneration sites of the lumbar spinal tissue at the remission stage. In addition to the normal-appearing paranodal myelin, we also observed retracted paranodal myelin [Fig. 9(a)] and split paranodal myelin [Fig. 9(b)] with thinner internodal myelin. Consistent with CARS imaging of paranodal myelin, immunolabels of Kv1.2 channels displayed both typical pairs [Fig. 9(c)] and redistribution of channels [Fig. 9(d)]. The morphology of NFC2 labeling appeared to be normal [Figs. 9(e) and 9(f)].

Quantitative measurements of nodal length over nodal diameter revealed mixed populations of normal nodes and elongated exposed nodes [Fig. 9(g)]. The mean ratio of nodal length to nodal diameter was significantly reduced during remission in comparison to that at the border of lesions during peak acute, while still significantly higher than that in the naive white matter [Fig. 9(h)]. Moreover, quantitative analysis of NFC2 labeling showed a significant length increase in all stages of R-EAE compared to the naive white matter [Figs. 9(i) and 9(j)]. Together, these results indicate an incomplete restoration of paranodal structure in the regenerating process.

4 Discussion

To date, it is still elusive how the myelin is degraded in multiple sclerosis.[32–35] There are two possible scenarios of demyelination
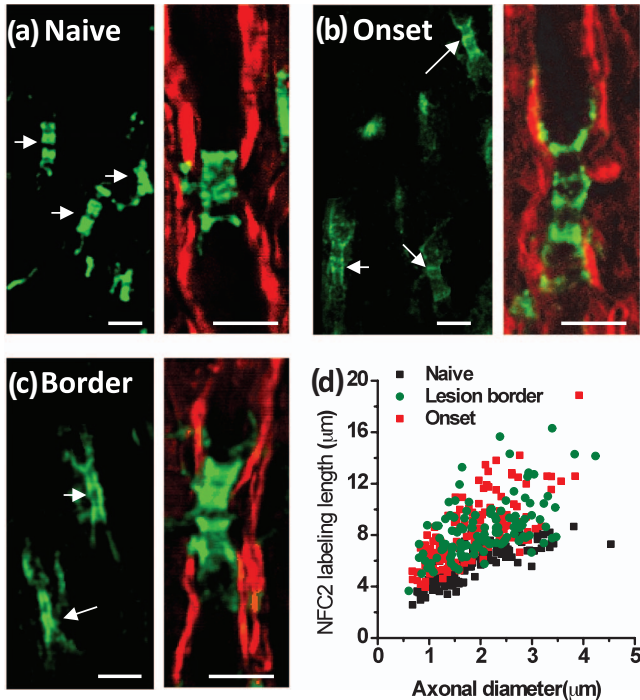
Fig. 7 Elongated neurofascin distribution in the paranodal domain. Green: immunolabeled NFC2 imaged by TPEF; red: myelin imaged by CARS. (a–c) Representative images of labeled NFC2 representing neurofascin 155 at the paranodal myelin and neurofascin 186 at the nodal axolemma in the white matter of naïve, EAE onset, and lesion borders at peak acute EAE. Elongated distribution of NFC2 was observed with extension into the internodes at locations no more than 100 μm away from the meninges at EAE onset and within lesion borders at peak acute EAE. (d) Comparison of NFC2 labeling lengths versus axonal diameters at different stages. Bar = 5 μm.
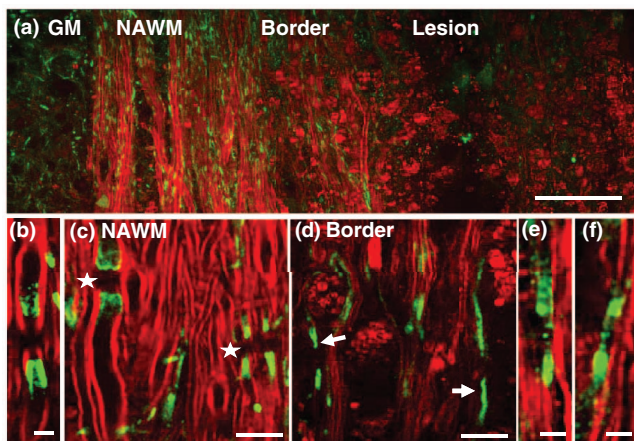

Fig. 8 Exposure and displacement of juxtaparanodal Kv1.2 channels. Red: myelin imaged by CARS; green: immunolabeled Kv1.2 channels imaged by TPEF. (a) Mosaic image showing a large view of Kv1.2 labeling and myelin in a lumbar spinal slice at the peak acute EAE. (b) A typical image of paired Kv1.2 channels in the naive white matter that are located at the juxtaparanodes and concealed beneath the compact myelin. (c) NAWM at the peak acute EAE showing paired Kv1.2 labeling (stars) under the myelin cover. (d, e) Exposed Kv1.2 channels [arrows in (d)] and displacement of Kv1.2 channels into the paranodes and nodes at the border of demyelinating lesions. In the lesions where myelin debris was present, no paired Kv1.2 channels were observed. (f) Exposure and displacement of Kv1.2 channels in the white matter of EAE onset. Bar = 50 μm in (a); bar = 5 μm in (b, e, f); bar = 10 μm in (c, d).

based on previous studies. The first one is injury starting from internodal myelin, for example, thinning of internodal myelin layer by layer, as observed in lysolecithin-induced myelin swelling.[19,36] The second one initiates with paranodal domain injury.[7,9] In this study, CARS microscopy has been employed to examine these scenarios by label-free mapping of single myelin fibers in different clinical scores (0, 1, and 3) of R-EAE. With submicron spatial resolution, the CARS images allowed us to quantify the myelin thickness and determine the ratio of myelin thickness to the axonal diameter in different stages of the disease. Furthermore, by coupling CARS with two-photon immunofluorescence mapping of juxtaparanodal K^+ channels, paranodal myelin retraction, and displacement of K^+ channels are extensively observed at the onset of R-EAE and at the lesion border. Our results show that the loss of nodal integrity precedes the formation of myelin debris in a strict $CD4^+$ T-cell-mediated R-EAE model of MS and that remyelination is accompanied by reestablishment of the nodal markers. Further experiments will be carried out by using *in vivo* imaging techniques to explore the demyelination sequences on single axons. Correlating our imaging results with the clinical scores demonstrates that alterations of the delicate nodal organization can disrupt axonal conduction in the onset stage of R-EAE. In addition, our finding that paranodal myelin is only partially restored in the regenerating sites offers one possible explanation to the incomplete functional recovery at the remission stage. We note that the relevance of this scenario of initiation of myelin destruction to that occurring in MS, which appears to be a collection of distinct histopathological subtypes,[37] remains to be determined by further studies.

Understanding the mechanism underlying the disruption of paranodal myelin is important for the development of therapies aimed at delaying or preventing disease relapses. In the inflammatory lesions, infiltrating immune cells release proinflammatory cytokines, including IFN-γ, TNF-α, IL-17, GM-CSF, and LT, and numerous chemokines including RANTES, IP-10 and IL-8.[11] These proinflammatory cytokines and chemokines are able to activate resident astrocytes and microglia cells,[11] which then produce nitric oxide and oxygen radicals[38,39] and glutamate,[40,41] leading to white matter damage.[42] Glutamate excitotoxicity has been shown to contribute to oligodendrocyte damage through glutamate receptors in the EAE model.[43] Our previous work has shown that a high level of glutamate is able to inflict paranodal myelin splitting and retraction through NMDA and kainate receptor-mediated calcium influx.[20] The similarity of structural changes suggests glutamate excitotoxicity as a possible mechanism contributing to the early myelin damage in the SJL R-EAE model. Indeed, the administration of glutamate receptor inhibitor before the onset of EAE has been shown to improve the neurological outcome and delay the progression of EAE.[43,44] The partial restoration of paranodal myelin shown in Fig. 9 may be related to the abnormal interactions between oligodendrocytes and axons[29] during remyelination. Our result highlights the significance of not only promoting remyelination, but also recovering the paranodal domain in myelin repair therapy.

With label-free vibrational contrast, 3-D submicron resolution, multimodality, and live-animal imaging capability,[45,46] CARS microscopy is expected to have wide applications to myelin biology. Initial applications have revealed the role of glutamate excitotoxicity in paranodal myelin damage.[20] Such
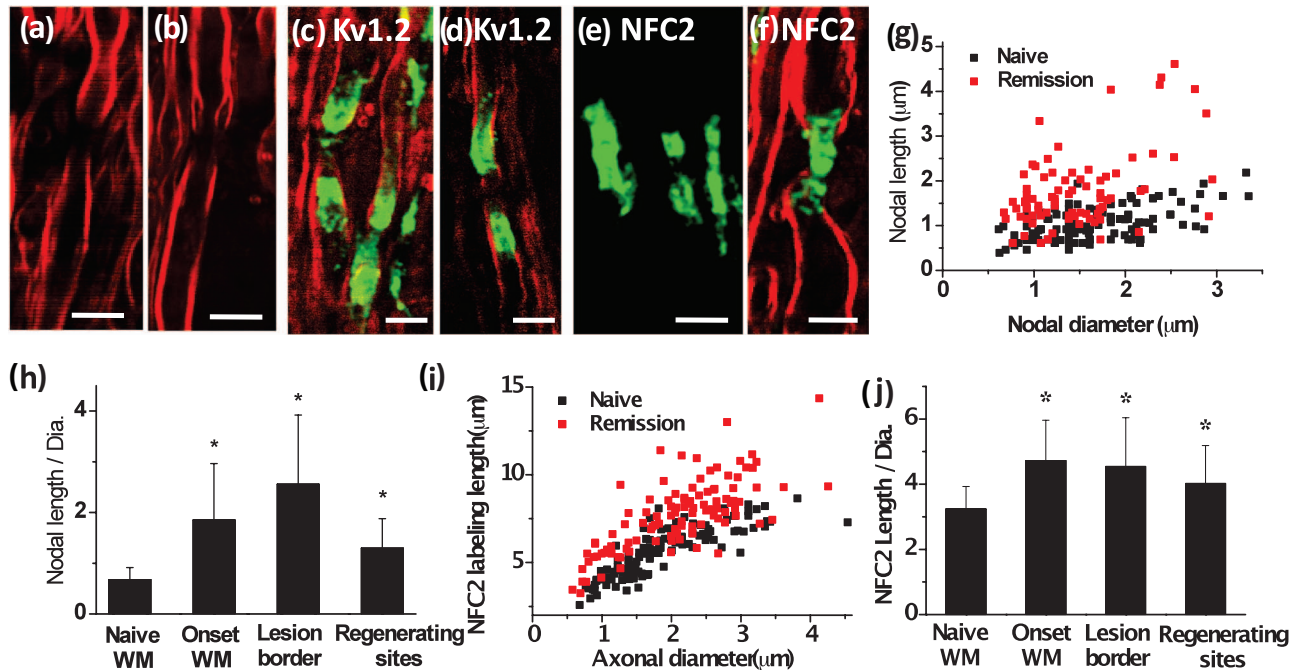
Fig. 9 Paranodal myelin is partially restored at remission stage. (a,b) CARS images of paranodal myelin in the regenerating sites at the remission stage. Retracted paranodal myelin (a) and split paranodal myelin (b) were observed. (c, d) Overlaid TPEF image of Kv1.2 channels (green) and CARS image of myelin (red) in the regenerating sites. Normal Kv1.2 channel pair (c) and displacement of Kv1.2 channels into the paranodes and nodes (d) were observed. (e) TPEF image of NFC2 labels in a regenerating site. (f) Overlaid TPEF image of NFC2 labels and CARS image of myelin in a regenerating site. The NFC2 labels were normally embedded into two segments of thinner myelin. (g) Comparison of nodal lengths versus nodal diameters based on the CARS images of paranodal myelin. (h) Comparison of ratios of nodal length to nodal diameter at different stages of EAE. (i) NFC2 labeling lengths at the regenerating sites versus naïve white matter. (j) Comparison of NFC2 lengths at different stages of EAE. In (h, j), $*p < 0.001$ compared to those in the naïve white matter. Bar = 5 μm.

capabilities can be extended to investigate the roles of oxidative stress and nitric oxide in myelin loss.[42] Furthermore, CARS imaging can be coupled with genetic tools to explore the roles of specific myelin components, such as the galactolipid,[29,47] and axonal proteins, such as AnkyrinG,[48] Caspr/paranodin,[49] and neurofascin proteins[50] in the organization of paranodal and nodal domains.[51] Finally, CARS microscopy can be used as a reliable and efficient readout of de- and remyelination in demyelinating diseases. Recent efforts have been made to promote remyelination by using γ secretase inhibitor in the coculture system[52] and EAE mice.[53] With *in vivo* imaging capabilities,[21,45,54] CARS microscopy would effectively allow quantitation of the outcome of the myelin repair therapies.

References

1. S. Poliak and E. Peles, "The local differentiation of myelinated axons at nodes of Ranvier," *Nat. Rev. Neurosci.* **4**, 968–980 (2003).
2. J. A. Black, J. D. Kocsis, and S. G. Waxman, "Ion channel organization of the myelinated fiber," *Trends Neurosci.* **13**, 48–54 (1990).
3. S. Tait, F. Gunn-Moore, J. M. Collinson, J. Huang, C. Lubetzki, L. Pedraza, D. L. Sherman, D. R. Colman, and P. J. Brophy, "An oligodendrocyte cell adhesion molecule at the site of assembly of the paranodal axo-glial junction," *J. Cell Biol.* **150**, 657–666 (2000).
4. P. Charles, S. Tait, C. Faivre-Sarrailh, G. Barbin, F. Gunn-Moore, N. Denisenko-Nehrbass, A. Guennoc, J. Girault, P. J. Brophy, and C. Lubetzki, "Neurofascin is a glial receptor for the paranodin/Caspr-contactin axonal complex at the axoglial junction," *Curr. Biol.* **12**, 217–220 (2002).
5. A. Van Wart, T. Boiko, J. S. Trimmer, and G. Matthews, "Novel clustering of sodium channel Na$_v$ 1.1 with ankyrin-G and neurofascin at discrete sites in the inner plexiform layer of the retina," *Mol. Cell. Neurosci.* **28**, 661–673 (2005).
6. S. Lambert, J. Q. Davis, and V. Bennett, "Morphogenesis of the node of ranvier: co-clusters of ankyrin and ankyrin-binding integral proteins define early developmental intermediates," *J. Neurosci.* **17**, 7025–7036 (1997).
7. O. W. Howell, A. Palser, A. Polito, S. Melrose, B. Zonta, C. Scheiermann, A. J. Vora, P. J. Brophy, and R. Reynolds, "Disruption of neurofascin localization reveals early changes preceding demyelination and remyelination in multiple sclerosis," *Brain* **129**, 3173–3185 (2006).
8. G. Wolswijk and R. Balesar, "Changes in the expression and localization of the paranodal protein Caspr on axons in chronic multiple sclerosis," *Brain* **126**, 1638–1649 (2003).
9. I. Coman, M. S. Aigrot, D. Seilhean, R. Reynolds, J. A. Girault, B. Zalc, and C. Lubetzki, "Nodal, paranodal and juxtaparanodal axonal proteins during demyelination and remyelination in multiple sclerosis," *Brain* **129**, 3186–3195 (2006).
10. R. Martin and S. Dhib-Jalbut, *Multiple Sclerosis: Diagnosis, Medical Management, and Rehabilitation*, Demos Medical Publishing, New York (2000).
11. M. Sospedra and R. Martin, "Immunology of multiple sclerosis," *Annu. Rev. Immunol.* **23**, 683–747 (2005).
12. A. M. Ercolini and S. D. Miller, "Mechanisms of immunopathology in murine models of central nervous system demyelinating disease," *J. Immunol.* **176**, 3293–3298 (2006).
13. T. J. Frederick and S. D. Miller, "Future of multiple sclerosis therapy: combining antigen-specific immunotherapy with strategies to promote myelin repair," *Future Neurol.* **1**, 489–503 (2006).

14. R. Gold, C. Linington, and H. Lassmann, "Understanding pathogenesis and therapy of multiple sclerosis via animal models: 70 years of merits and culprits in experimental autoimmune encephalomyelitis research," *Brain* **129**, 1953–1971 (2006).

15. D. W. Paty, D. K. B. Li, J. J.-F. Oger, L. Kastrukoff, R. Koopmans, E. Tanton, and G. J. Zhao, "Magnetic resonance imaging in the evaluation of clinical trials in multiple sclerosis," *Ann. Neurol.* **36**, S95–S96 (1994).

16. B. Stankoff, Y. Wang, M. Bottlaender, M.-S. Aigrot, F. Dolle, C. Wu, D. Feinstein, G.-F. Huang, F. Semah, C. A. Mathis, W. Klunk, R. M. Gould, C. Lubetzki, and B. Zalc, "Imaging of CNS myelin by positron-emission tomography," *Proc. Natl. Acad. Sci. U S A* **103**, 9304–9309 (2006).

17. J. X. Cheng, A. Volkmer, and X. S. Xie, "Theoretical and experimental characterization of coherent anti-Stokes Raman scattering microscopy," *J. Opt. Soc. Am. B* **19**, 1363–1375 (2002).

18. H. Wang, Y. Fu, P. Zickmund, R. Shi, and J. X. Cheng, "Coherent anti-Stokes Raman scattering imaging of live spinal tissues," *Biophys. J.* **89**, 581–591 (2005).

19. Y. Fu, H. Wang, T. B. Huff, R. Shi, and J. X. Cheng, "Coherent anti-Stokes Raman scattering imaging of myelin degradation reveals a calcium dependent pathway in lyso-PtdCho induced demyelination," *J. Neurosci. Res.* **85**, 2870–2881 (2007).

20. Y. Fu, W. Sun, Y. Shi, R. Shi, and J. X. Cheng, "Glutamate excitotoxicity inflicts paranodal myelin splitting and retraction," *PLoS ONE* **4**(8), e6705 (2009).

21. F. P. Henry, D. Cote, M. A. Randolph, E. A. Z. Rust, R. W. Redmond, I. E. Kochevar, C. P. Lin, and J. M. Winograd, "Real-time *in vivo* assessment of the nerve microenvironment with coherent anti-Stokes Raman scattering microscopy," *Plast. Reconstruct. Surg.* **123**, 123s–130s (2009).

22. E. Belanger, S. Begin, S. Laffray, Y. D. Koninck, R. Vallee, and D. Cote, "Quantitative myelin imaging with coherent anti-Stokes Raman scattering microscopy: alleviating the excitation polarization dependence with circularly polarized laser beams," *Opt. Express* **17**, 18419–18432 (2009).

23. M. Slipchenko, T. T. Le, H. Chen, and J. X. Cheng, "Compound Raman microscopy for high-speed vibrational imaging and spectral analysis of lipid bodies," *J. Phys. Chem. B* **113**, 7681–7686 (2009).

24. G. Ayala, P. Carmona, M. de Cózar, and J. Monreal, "Vibrational spectra and structure of myelin membranes," *Eur. Biophys. J.* **14**, 219–225 (1987).

25. M. Pézolet and D. Georgescauld, "Raman spectroscopy of nerve fibers: a study of membrane lipids under steady state conditions," *Biophys. J.* **47**, 367–372 (1985).

26. B. Muik, B. Lendl, A. Molina-Díaz, and M. J. Ayora-Cañada, "Direct monitoring of lipid oxidation in edible oils by Fourier transform Raman spectroscopy," *Chem. Phys. Lipids* **134**, 173–182 (2005).

27. B. Ohler, K. Graf, R. Bragg, T. Lemons, R. Coe, C. Genain, J. Israelachvili, and C. Husted, "Role of lipid interactions in autoimmune demyelination," *Biochim. Biophys. Acta* **1688**, 10–17 (2004).

28. J. Q. Davis, S. Lambert, and V. Bennett, "Molecular composition of the node of Ranvier: identification of ankyrin-binding cell adhesion molecules neurofascin (mucin+/third FNIII domain-) and NrCAM at nodal axon segments," *J. Cell Biol.* **135**, 1355–1367 (1996).

29. J. L. Dupree, J. A. Girault, and B. Popko, "Axo-glial interactions regulate the localization of axonal paranodal proteins," *J. Cell Biol.* **147**, 1145–1152 (1999).

30. H. Wang, D. D. Kunkel, T. M. Martin, P. A. Schwartzkroin, and B. L. Tempel, "Heteromultimeric K$^+$ channels in terminal and juxtaparanodal regions of neurons," *Nature* **365**, 75–79 (1993).

31. K. J. Rhodes, B. W. Strassle, M. M. Monaghan, Z. Bekele-Arcuri, M. F. Matos, and J. S. Trimmer, "Association and colocalization of the Kvβ1 and Kvβ2 β-subunits with Kv1 α-subunits in mammalian brain K$^+$ channel complexes," *J. Neurosci.* **17**, 8246–8258 (1997).

32. R. A. Lazzarini, Ed., *Myelin Biology and Its Disorders*, Elsevier Academic Press, San Diego (2004).

33. B. D. Trapp, J. Peterson, R. M. Ransohoff, R. Rudick, S. Mörk, and L. Bö, "Axonal transection in the lesions of multiple sclerosis," *New Engl. J. Med.* **338**, 278–285 (1998).

34. H. Lassmann, "Axonal injury in multiple sclerosis," *J. Neurol. Neurosurg. Psychiatry* **74**, 695–697 (2003).

35. M. H. Barnett, A. P. Henderson, and J. W. Prineas, "The macrophage in MS: just a scavenger after all? Pathology and pathogenesis of the acute MS lesion," *Multiple Sclerosis* **12**, 121–132 (2006).

36. S. M. Hall and N. A. Gregson, "The *in vivo* and ultrastructrual effects of injection of lysophosphatidyl choline into myelinated peripheral nerve fibers of the adult mouse," *J. Cell Sci.* **9**, 769–789 (1971).

37. C. Lucchinetti, W. Brück, J. Parisi, B. Scheithauer, M. Rodriguez, and H. Lassmann, "Heterogeneity of multiple sclerosis lesions: implications for the pathogenesis of demyelination," *Ann. Neurol.* **47**, 707–717 (2000).

38. Y. Gilgun-Sherki, E. Melamed, and D. Offen, "The role of oxidative stress in the pathogenesis of multiple sclerosis: the need for effective antioxidant therapy," *J. Neurol.* **251**, 261–268 (2004).

39. Y. Nomura, "NF-kappaB activation and IkappaB alpha dynamism involved in iNOS and chemokine induction in astroglial cells," *Life Sci.* **68**, 1695–1701 (2001).

40. H. Takeuchi, T. Mizuno, G. Zhang, J. Wang, J. Kawanokuchi, R. Kuno, and A. Suzumura, "Neuritic beading induced by activated microglia is an early feature of neuronal dysfunction toward neuronal death by inhibition of mitochondrial respiration and axonal transport," *J. Biol. Chem.* **280**, 10444–10454 (2005).

41. C. M. Anderson and R. A. Swanson, "Astrocyte glutamate transport: review of properties, regulation, and physiological functions," *Glia* **32**, 1–14 (2000).

42. P. K. Stys, "White matter injury mechanisms," *Curr. Mol. Med.* **4**, 113–130 (2004).

43. D. Pitt, P. Werner, and C. S. Raine, "Glutamate excitotoxicity in a model of multiple sclerosis," *Nat. Med.* **6**, 67–70 (2000).

44. T. Smith, A. Groom, B. Zhu, and L. Turski, "Autoimmune encephalomyelitis ameliorated by AMPA antagonists," *Nat. Med.* **6**, 62–66 (2000).

45. Y. Fu, T. B. Huff, H. W. Wang, H. Wang, and J. X. Cheng, "Ex vivo and in vivo imaging of myelin fibers in mouse brain by coherent anti-Stokes Raman scattering microscopy," *Opt. Express* **16**, 19396–19409 (2008).

46. T. Hellerer, C. Axäng, C. Brackmann, P. Hillertz, M. Pilon, and A. Enejder, "Monitoring of lipid storage in *Caenorhabditis* elegans using coherent anti-Stokes Raman scattering (CARS) microscopy," *Proc. Nat. Acad. Sci. U S A* **104**, 14658–14663 (2007).

47. J. L. Dupree, T. Coetzee, A. Blight, K. Suzuki, and B. Popko, "Myelin galactolipids are essential for proper node of Ranvier formation in the CNS," *J. Neurosci.* **18**, 1642–1649 (1998).

48. D. Zhou, S. Lambert, P. L. Malen, S. Carpenter, L. M. Boland, and V. Bennett, "AnkyrinG is required for clustering of voltage-gated Na channels at axon initial segments and for normal action potential firing," *J. Cell. Biol.* **143**, 1295–1304 (1998).

49. M. A. Bhat, J. C. Rios, Y. Lu, G. P. Garcia-Fresco, W. Ching, M. St Martin, J. Li, S. Einheber, M. Chesler, J. Rosenbluth, J. L. Salzer, and H. J. Bellen, "Axon-glia interactions and the domain organization of myelinated axons requires neurexin IV/Caspr/Paranodin," *Neuron* **30**, 369–383 (2001).

50. D. L. Sherman, S. Tait, S. Melrose, R. Johnson, B. Zonta, F. A. Court, W. B. Macklin, S. Meek, A. J. H. Smith, D. F. Cottrell, and P. J. Brophy, "Neurofascins are required to establish axonal domains for saltatory conduction," *Neuron* **48**, 737–742 (2005).

51. J. A. Girault and E. Peles, "Development of nodes of Ranvier," *Curr. Opin. Neurobiol.* **12**, 476–485 (2002).

52. T. A. Watkins, B. Emery, S. Mulinyawe, and B. A. Barres, "Distinct stages of myelination regulated by gamma-secretase and astrocytes in a rapidly myelinating CNS coculture system," *Neuron* **60**, 555–569 (2008).

53. L. M. Minter, D. M. Turley, P. Das, H. M. Shin, I. Joshi, R. G. Lawlor, O. H. Cho, T. Palaga, S. Gottipati, J. C. Telfer, L. Kostura, A. H. Fauq, K. Simpson, K. A. Such, L. Miele, T. E. Golde, S. D. Miller, and B. A. Osborne, "Inhibitors of γ-secretase block *in vivo* and *in vitro* T helper type 1 polarization by preventing Notch upregulation of *Tbx21*," *Nat. Immnuol.* **6**, 680–688 (2005).

54. T. B. Huff and J. X. Cheng, "*In vivo* coherent anti-Stokes Raman scattering imaging of sciatic nerve tissue," *J. Microsc.* **225**, 175–182 (2007).